

# Rheology of mobile sediment beds sheared by viscous, pressure-driven flows

B. Vowinckel<sup>1,2,†</sup>, E. Biegert<sup>1</sup>, E. Meiburg<sup>1</sup>, P. Aussillous<sup>3</sup> and É. Guazzelli<sup>4</sup>

<sup>1</sup>Department of Mechanical Engineering, University of California Santa Barbara, Santa Barbara, CA 93106, USA

<sup>2</sup>Leichtweiß-Institute for Hydraulic Engineering and Water Resources, Technische Universität Braunschweig, 38106 Braunschweig, Germany

<sup>3</sup>Aix Marseille Université, CNRS, IUSTI, Marseille, France

<sup>4</sup>Université de Paris, CNRS, Matière et Systèmes Complexes (MSC) UMR 7057, Paris, France

(Received 18 October 2020; revised 26 February 2021; accepted 7 May 2021)

We present a detailed comparison of the rheological behaviour of sheared sediment beds in a pressure-driven, straight channel configuration based on data that were generated by means of fully coupled, grain-resolved direct numerical simulations and experimental measurements previously published by Aussillous *et al.* (*J. Fluid Mech.*, vol. 736, 2013, pp. 594–615). The highly resolved simulation data allow us to compute the stress balance of the suspension in the streamwise and vertical directions and the stress exchange between the fluid and particle phases, which is information needed to infer the rheology, but has so far been unreachable in experiments. Applying this knowledge to the experimental and numerical data, we obtain the statistically stationary, depth-resolved profiles of the relevant rheological quantities. The scaling behaviour of rheological quantities such as the shear and normal viscosities and the effective friction coefficient are examined and compared to data coming from rheometry experiments and from widely used rheological correlations. We show that rheological properties that have previously been inferred for annular Couette-type shear flows with neutrally buoyant particles still hold for our set-up of sediment transport in a Poiseuille flow and in the dense regime we found good agreement with empirical relationships derived therefrom. Subdividing the total stress into parts from particle contact and hydrodynamics suggests a critical particle volume fraction of 0.3 to separate the dense from the dilute regime. In the dilute regime, i.e. the sediment transport layer, long-range hydrodynamic interactions are screened by the porous medium and the effective viscosity obeys the Einstein relation.

**Key words:** sediment transport, rheology, suspensions

† Email address for correspondence: [b.vowinckel@tu-braunschweig.de](mailto:b.vowinckel@tu-braunschweig.de)

© The Author(s), 2021. Published by Cambridge University Press. This is an Open Access article, distributed under the terms of the Creative Commons Attribution licence (<http://creativecommons.org/licenses/by/4.0/>), which permits unrestricted re-use, distribution, and reproduction in any medium, provided the original work is properly cited.

## 1. Introduction

Understanding and predicting the behaviour of mobile, granular sediment beds exposed to shearing flows is essential for a number of natural phenomena (e.g. sediment transport in rivers and oceans) but also for numerous engineering processes (e.g. slurry transport in the mining and petroleum industries). While many of these flows are turbulent, this is not always the case, and laminar flows are also present in many situations, such as the debris flow of highly concentrated suspensions or the creeping motion of soils down a hill slope (Jerolmack & Daniels 2019). The underlying physical mechanisms leading to the morphology of sediment beds, i.e. ripples and dunes, observed in the turbulent case seem also to bear many similarities to those seen in the laminar case (Lajeunesse *et al.* 2010). Studies for laminar cases can thus be important to create analogues of phenomena that occur in turbulent flows at larger field scales but are also of interest by themselves. The present study focuses on this laminar regime.

Modelling sediment transport requires the understanding of the rheological behaviour of the granular material (Vowinckel 2021, and references therein). Gravity plays an important role as it controls the level of stress experienced by the grains. The motion of the grains is caused by the shearing forces exerted by the fluid at the surface of the sedimented bed but the grain packing is controlled by gravity and is free to dilate as the shearing forces are increased. This rheological situation, termed pressure imposed, has been the subject of significant recent advances. It has been shown that a description in terms of a frictional rheology can be applied to both dry granular flows and viscous suspensions, despite the fact that the interactions between particles may be different. Inter-particle collisions and friction between contacting particles dominate in granular flow while hydrodynamic interactions are important in viscous suspension although the role of contacts becomes increasingly predominant with increasing concentration (see e.g. Guazzelli & Pouliquen 2018).

In the inertial case of a dry granular material sheared at a shear rate  $\dot{\gamma}$  under an imposed granular pressure  $p_p$ , the rheology is determined by the particle volume fraction,  $\phi$ , and the macroscopic friction,  $\mu = \tau/p_p$ , where  $\tau$  is the shear stress, which both are functions of a single dimensionless inertial number  $I = d_p \dot{\gamma} \sqrt{\rho_p/p_p}$ , where  $d_p$  is the particle diameter and  $\rho_p$  the particle density (GDR Midi 2004; Forterre & Pouliquen 2008). A similar formalism can be applied to viscous suspensions of non-Brownian spheres but with a viscous number  $J = \eta_f \dot{\gamma}/p_p$  in place of the inertial number  $I$  (Boyer, Guazzelli & Pouliquen 2011), where  $\eta_f$  is the dynamic viscosity. This frictional formulation is equivalent to the more classical presentation using viscosities depending solely on  $\phi$ , where the relative shear and normal viscosities can be obtained as  $\eta_s = \tau/\eta_f \dot{\gamma} = \mu/J$  and  $\eta_n = p_p/\eta_f \dot{\gamma} = 1/J$ . The transition from the viscous to the inertial regime is far from being completely understood but is supposed to occur when the Stokes number  $St = I^2/J = \rho_p \dot{\gamma} d_p^2/\eta_f$  is  $\sim O(1-10)$  (Bagnold 1954; Ness & Sun 2015).

Traditionally, the rheology of dense suspensions has been assessed in rheometry experiments of neutrally buoyant spheres, by imposing a constant volume fraction,  $\phi$ , to obtain the shear viscosity  $\eta_s$  as a function of  $\phi$  (see e.g. Stickel & Powell 2005; Guazzelli & Pouliquen 2018). The pressure-imposed rheometry described in the preceding paragraphs is a recent addition and has been found to be particularly useful in the range of large  $\phi$ , which is less amenable to conventional rheometry (Boyer *et al.* 2011; Dagois-Bohy *et al.* 2015; Guazzelli & Pouliquen 2018; Tapia, Pouliquen & Guazzelli 2019). This latter approach where the suspension is free to expand (or to contract) under shear is particularly well suited to study the rheology close to the jamming transition and to measure the

maximum volume fraction,  $\phi_c$ , where the viscosities diverge. Another valuable aspect of this pressure-controlled rheometry is the direct measurement of the particle pressure,  $p_p$ , which is usually not accessible to conventional rheometry.

The rheological measurements can be described by empirical correlations relating the shear viscosity,  $\eta_s$ , to the volume fraction,  $\phi$  (see e.g. Stickel & Powell 2005). There are also phenomenological relations for the normal viscosity,  $\eta_n$ , vs  $\phi$ , in particular that proposed by Morris & Boulay (1999) to match experimental results on shear-induced migration. Of particular interest to sediment transport, wherein two different phases need to be addressed, are the relations proposed by Boyer *et al.* (2011) as the expressions for  $\mu(J)$  and  $\phi(J)$  and equivalently for  $\eta_s(\phi)$  and  $\eta_n(\phi)$  that contain two terms, one coming from the hydrodynamic interactions and one coming from direct contacts. The viscous term is constructed to yield the Einstein viscosity at low  $\phi$  while the contact term is similar to that found for dry granular media and produces the observed power-law divergence at the jamming transition. It is important to note that these phenomenological relations are inherently empirical, because they involve adjustable parameters that have been determined by best fit to experimental data of sheared dense suspensions with particle volume fractions  $\phi/\phi_c > 0.5$ . Hence, using these correlations to describe sediment transport may be problematic, because the bed-load transport layer can easily reach values lower than the data range of the rheometry experiments. Consequently, there is a need to investigate sediment transport by means of highly resolved data to test the validity of the empirical correlations as constitutive laws.

Modelling sediment flows on a continuum scale indeed requires application of a two-phase approach, and thus use of the appropriate constitutive relationships for the stresses of the fluid and particle phases is essential. This search started with the pioneering studies of Bagnold (1956), who applied the results of his rheological experiments (Bagnold 1954) to the non-uniform case of grains flowing over a gravity bed, i.e. a sediment bed stabilised by gravity. Recognising the necessity of a frictional view of the problem has been found to be instrumental. In particular, Ouriemi, Aussillous & Guazzelli (2009) used a frictional rheology similar to that proposed for dry granular media to describe the stress of the particle phase as they considered that the grains were mainly interacting through contact forces inside the bed. They also took a Newtonian rheology for the fluid phase with an Einstein dilute viscosity, as for grains in contact higher-order hydrodynamic interactions are shielded and the viscosity reduced to its dilute value.

Two-phase modelling using a  $\mu(J)$  frictional rheology has been tested against bed-load experiments in channel flows by Aussillous *et al.* (2013) and was found to be successful in predicting the flow inside the mobile bed. However, the rheological coefficients were adjusted to match the experimental velocity and concentration profiles and overall differ from those found by Boyer *et al.* (2011). Another method followed by Houssais *et al.* (2016) was to consider heavy particles sheared in an annular channel and to infer the rheological properties of the settled suspension. The rheology of Boyer *et al.* (2011) was recovered, but with the addition of a pressure at the interface of the free-fluid flow and the sediment bed, which corresponded to some fraction of the weight of an individual particle. These experiments, which aim at studying the rheological behaviour of mobile sediment beds, are particularly difficult as they require great accuracy in the measurements of the packing fraction and of both the particle and fluid motion. There are additional difficulties coming from the choice of the shearing flows. In annular Couette flows (Mouilleron, Charru & Eiff 2009; Houssais *et al.* 2016), the thickness of the flowing suspension is merely two particle diameters, and using a continuum description may

not be fully justified. The mobile layer is much thicker in Poiseuille-type flows and is better suited to a comparison with a continuum modelling. This set-up is also a more realistic representation of a natural channel because, unlike in annular flows, the sidewalls have no curvature (Lobkovsky *et al.* 2008; Aussillous *et al.* 2013; Allen & Kudrolli 2017). However, using a straight channel configuration may also prove to be problematic as there is a continuous erosion in the channel, and consequently the generated data always contain a transient component where erosion and deposition may not be in full equilibrium.

Consequently, uncertainties remain as to how rheological models derived for Couette flows are applicable to the situation of natural sediment transport, where the flow is typically driven by a volume force, such as a pressure gradient or a downhill force. For these types of flows, the key differences are (i) total shear increasing with flow depth, which yields a wide range of viscous numbers  $J$ , (ii) settled particles where the particle pressure  $p_p$  and viscous number  $J$  vary vertically and (iii) non-homogeneous particle volume fractions throughout the bed-load transport layer at the interface between the free-fluid flow and the sediment bed. In particular, this latter region close to the interface remains poorly accessible by means of experimental measuring techniques. A promising alternative route for investigating the rheological behaviour of sediment beds is to use direct numerical simulations (DNS) at the particle scale. There are only a few contributions in the context of bed-load transport. In particular, the study of Kidanemariam & Uhlmann (2014), which uses the immersed boundary method (IBM) for the fluid-solid coupling and a soft-sphere approach for solid–solid contact (discrete element models (DEM)), investigated the flow-induced motion of a thick bed of spherical particles and found excellent agreement with the mean flow properties reported by Aussillous *et al.* (2013) even though the Reynolds number in the simulations was two orders of magnitude larger than in the experiment. Furthermore, Kidanemariam (2016) presented a first attempt to directly infer the rheology of a sheared sediment bed. The present paper is following this route to verify if previous rheological considerations from pressure-imposed rheometry remain applicable for the set-up of sediment transport in a pressure-driven flow.

The objective of the present contribution is, hence, to quantify the stress exchange of the fluid and particle phases in the mixture to access the highly complex fluid particle interactions in the bed-load transport layer. This analysis is crucial to compute directly the rheological behaviour of sediment beds exposed to a pressure-driven flow and allows for a comparison to previous rheological studies of annular Couette flows with neutrally buoyant particles. Towards this goal, we employ particle-resolved DNS using the IBM (Uhlmann 2005; Kempe & Fröhlich 2012a) and the DEM validated by Biegert, Vowinckel & Meiburg (2017a). The simulation framework is applied to reproduce the experimental configuration of Aussillous *et al.* (2013), albeit for higher flow rates but by still remaining in the viscous regime of flow with  $St < 10$ , see §§ 2 and 3. We then apply in § 4 the strategy of Biegert *et al.* (2018) and Vowinckel *et al.* (2019) to capture quantities unreachable in experiments such as the stress balances for the fluid and particle phases and the whole fluid–particle mixture in the streamwise and vertical directions. Rheological quantities are also inferred from these highly resolved data and are compared to the reconstructed rheological data from the experimental data of Aussillous *et al.* (2013) in § 5. The scaling behaviour of the shear and normal viscosities as well as of the effective friction coefficient are explored and compared to the data of Boyer *et al.* (2011), Dagois-Bohy *et al.* (2015) and Tapia *et al.* (2019) obtained by pressure-imposed rheometry as well as with widely used correlations (Morris & Boulay 1999; Boyer *et al.* 2011).

## 2. Experimental data

We use the experimental data of Aussillous *et al.* (2013) who examined the mobile layer of a granular bed in laminar flows in a rectangular-channel flow. This database yields depth-resolved profiles of particle velocity for a range of fluid heights  $h_f$  as the height of the clear-liquid layer above the granular bed and flow rates in the laminar regime.

We summarise below the main features of the experimental apparatus used to obtain this database. Further details can be found in Aussillous *et al.* (2013). Two batches of particles, consisting respectively of borosilicate spheres having a mean diameter  $d_p = 1.1 \pm 0.1$  mm and a specific density  $(\rho_p - \rho_f)/\rho_f = 1.1$  and of polymethyl methacrylate (PMMA) spheres having a mean diameter  $d_p = 2.04 \pm 0.03$  mm and a specific density  $(\rho_p - \rho_f)/\rho_f = 0.1$ , were selected, where  $\rho_f$  is the fluid density. The particles were immersed in a viscous fluid (mainly composed of Triton X-100 and water) having the same refractive index as the respective particles. A dye (Rhodamine 6G) that fluoresces when illuminated by the laser in the wavelength range greater than 555 nm was added to the fluid. The flow set-up consisted of a horizontal rectangular channel of length  $L_x = 100$  cm, height  $L_y = 6.5$  cm and width  $L_z = 3.5$  cm, where  $x$ ,  $y$  and  $z$  denote the streamwise, vertical and spanwise coordinates, respectively. To create a sediment bed, the channel was filled up with monodisperse particles and fluid, then turned upside down and tilted to consolidate the sediment bed. Afterwards, the channel was set horizontally and flipped back to its original position and a pressure gradient was applied to generate a small flow rate. This procedure was applied to fill solely the channel entrance with sedimented particles, leaving an empty buffer space near the outlet of the channel. A constant fluid flow rate,  $Q_f$ , was then applied to erode the sedimented bed of particles into the empty buffer space. In this way, the fluid shear stress at the top of the bed decreased as the fluid–particle interface (upstream from the buffer region) receded (i.e.  $h_f$  increased) with time. The fluid–sediment interface is detected by computing the maximum change of slope of the averaged grey level profile (green line in figure 1*a,c*). Several runs were conducted for each particle type, by varying the imposed flow rate. Data for the velocity profile (particle velocity,  $u_p$  and fluid velocity,  $u_f$ , in solely the pure fluid zone for the PMMA particles) were collected by averaging 10 images over 0.5 s every 5 s. In addition, bulk quantities were deduced such as the time evolution of the particle bed height,  $h_p$ , and the flow rate per unit width,  $q_{f,exp}$ , by neglecting the role of the moving granular layer. The experiments were conducted in the viscous regime with a Reynolds number defined as  $Re = \rho_f Q_f / \eta_f L_z$  in the range  $0.2 < Re < 1.2$ . The Stokes number based on the shear rate  $\dot{\gamma}$  was  $St = \rho_p d_p^2 \dot{\gamma} / \eta_f \approx 0.01$  on average.

The most difficult quantity to extract from the experiments is the particle volume fraction,  $\phi$ . In Aussillous *et al.* (2013), the volume-fraction profile for the borosilicate particles was evaluated by using the averaged grey-level profile,  $P_I(y)$ , of the same images as those utilised to infer the velocity profile and by scaling it by the grey-level profile of the immobile initial bed, which is assumed to be at the constant maximum particle volume fraction  $\phi_c = 0.585$ . However, the laser intensity was likely to have changed during a run and the maximum packing in the bed measured with this method was found to vary with the fluid height. We thus decided to revisit these data and to consider another method (also based on the averaged grey-level profile) to evaluate the volume fraction. As in Aussillous *et al.* (2013), we suppose that the grey-level intensity gradient is mainly due to a linear broadening of the laser line due to the use of a laser line generator with a finite fan angle (Dijksman *et al.* 2012). First, we adjust the intensity decay in the pure fluid zone by a linear function,  $P_I = P_{0I}(1 - y/y_0)$ , where  $P_{0I}$  and  $y_0$  are constants which depend on the laser and the fluid properties, see figure 1(*a,c*) corresponding respectively to run 1 and run



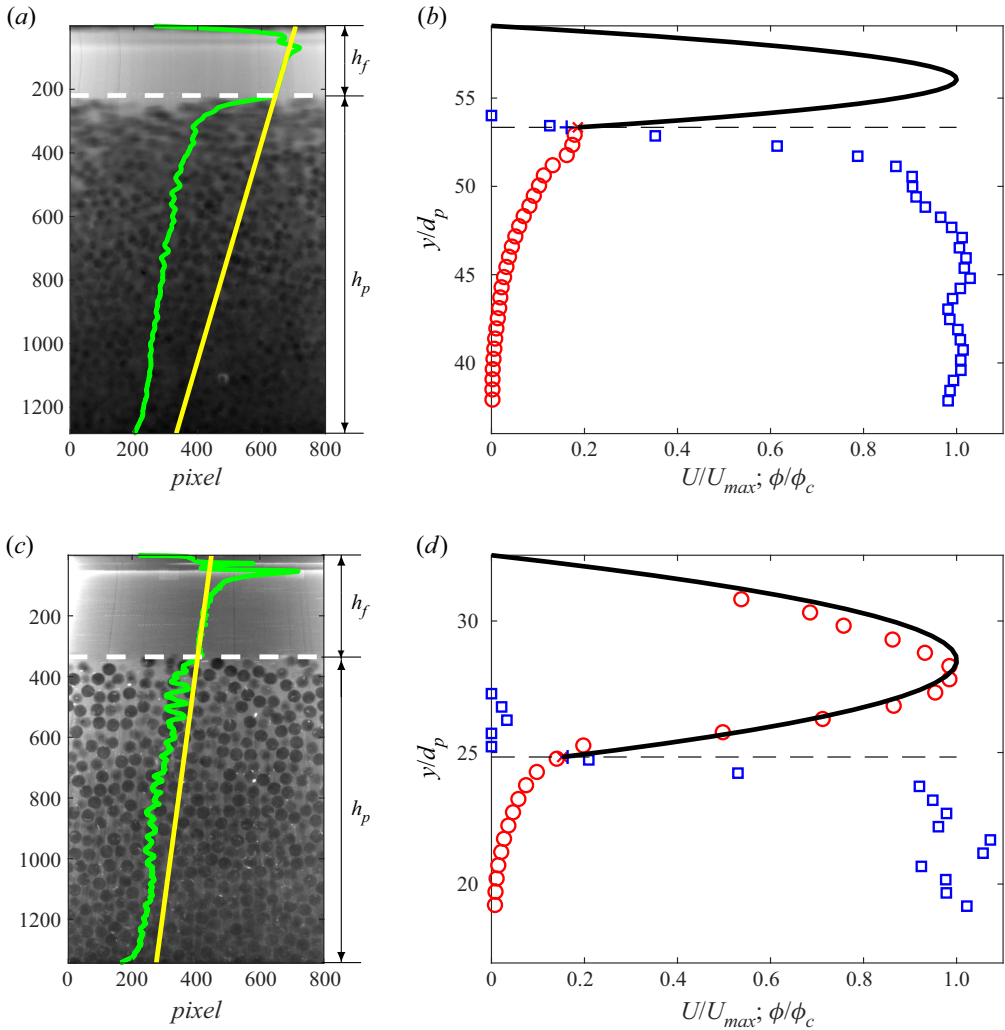


Figure 1. Depth-resolved quantities extracted from the experiments for (a,b) borosilicate particles with  $Q_f = 2.7 \times 10^{-6} \text{ m}^3 \text{ s}^{-1}$  and  $h_f = 6.3 \text{ mm}$  and for (c,d) PMMA particles with  $Q_f = 2.7 \times 10^{-6} \text{ m}^3 \text{ s}^{-1}$  and  $h_f = 15.3 \text{ mm}$  corresponding to runs 1 and 12 of Aussillous *et al.* (2013), respectively. (a,c) Averaged images over 10 s having a length scale (a)  $0.029 \text{ mm pixel}^{-1}$  and (b)  $0.046 \text{ mm pixel}^{-1}$  with the corresponding grey-level profile (green curve) and the linear adjustment in the pure fluid zone (yellow straight line). (b,d) Normalised volume-averaged velocity profile,  $U/U_{max}$  (red  $\circ$ ), and volume-fraction profile,  $\phi/\phi_c$  (blue  $\square$ ). The full line corresponds to the theoretical velocity profile in the pure fluid zone (2.3). The white and grey horizontal dashed lines in (a,c) and (b,d) respectively indicate the fluid–particle interface at  $y = h_p$ .

12 of Aussillous *et al.* (2013). Second, for the liquid–particle mixture we assume that  $P_I(y) = [(1 - \phi)P_{0l} + \phi P_{0s}](1 - y/y_0)$  where  $P_{0s}$  is related to the particle properties. We then introduce  $A = P_I(y)/(1 - y/y_0)$ , which is averaged over the same box size as that used for the velocity profile. If we suppose that  $\phi(h_c) = \phi_c$  and  $A(h_c) = A_c$  at the bottom of the mobile granular layer  $h_c$ , i.e. the height for which particle motion ceases, the volume fraction is given by  $\phi = \phi_c[A(y) - 1]/(A_c - 1)$ . In figure 1(b,d), we have plotted the normalised volume fraction,  $\phi/\phi_c$ , vs the vertical position made dimensionless using the particle diameter,  $y/d_p$ , for (b) borosilicate particles ( $Q_f = 2.7 \times 10^{-6} \text{ m}^3 \text{ s}^{-1}$  and

$h_f = 6.3$  mm) and (d) PMMA particles ( $Q_f = 2.7 \times 10^{-6}$  m<sup>3</sup> s<sup>-1</sup> and  $h_f = 15.3$  mm). We observe that the volume fraction increases rapidly downward from the fluid–particle interface and reaches quickly a constant value after approximately two sphere diameters.

To examine the rheological behaviour of the sheared sediment bed, we need to infer the depth-resolved shear rate,  $\dot{\gamma}$ , the mixture shear stress,  $\tau$ , and the particle pressure,  $p_p$ , from the particle velocity profile,  $u_p$ , and the volume-fraction profile,  $\phi$ . First, we interpolate linearly the velocity and volume-fraction profiles to obtain their value at the fluid–bed interface,  $u_{p,in}$  and  $\phi_{in}$ , see the red  $x$  and blue  $+$  on the dashed line in figure 1(b,d). The shear rate profile,  $\dot{\gamma}(y) = du_p/dy$ , is simply deduced numerically from the particle velocity profile using a second-order finite difference approximation. To evaluate the total shear stress and the particle pressure, we use the two-phase modelling developed in Aussillous *et al.* (2013). In this approach, a flat particle bed of thickness  $h_p$  is subjected to a Poiseuille flow driven by a pressure gradient,  $\partial p_f/\partial x$ , in a horizontal channel. The flow is assumed to be two-dimensional, stationary and uniform in the streamwise direction, also parallel and laminar. From the fluid phase equation (i.e. the Brinkman equation), the volume-averaged velocity in the horizontal  $x$ -direction is found to be  $U = \phi u_p + (1 - \phi) u_f \approx u_p \approx u_f$  in the bed due to the small permeability. In the laminar regime, the momentum equations for the mixture (particles plus fluid) then write

$$\tau(y) = \tau_f(h_p) - \frac{\partial p_f}{\partial x}(h_p - y), \tag{2.1}$$

$$\frac{\partial p_p}{\partial y} = \phi(y)\Delta\rho g, \tag{2.2}$$

where  $g$  is the gravitational acceleration and  $\Delta\rho = \rho_p - \rho_f$  corresponds to the density difference between the two phases. To compute the particle pressure profile inside the bed, (2.2) is integrated numerically along the vertical  $y$ -direction. It shows that the pressure of the particle phase is proportional to the apparent weight of the solid phase and increases when penetrating inside the bed. The total stress profile inside the bed is deduced from (2.1), provided the stresses applied by the fluid at the fluid/bed interface,  $\tau_f(h_p)$ , and the imposed fluid pressure gradient,  $\partial p_f/\partial x$ , are given.

Due to the lack of measurements of the fluid velocity in the pure fluid zone for the borosilicate particles, we need to reconstruct the fluid velocity profile for this batch of spheres based on the following assumptions:

- (i) The fluid velocity,  $u_f$ , is zero at the top wall ( $y = L_y$ ) and matches the particle velocity,  $u_{p,in}$ , at the bed height ( $y = h_p$ ).
- (ii) The fluid velocity profile is parabolic for  $y > h_p$  which yields the analytical solution for a mixed Couette–Poiseuille flow

$$u_f = \frac{\partial p_f/\partial x}{2\eta_f} (y^2 - L_y^2) - \left[ \frac{u_{p,in}}{h_f} + \frac{\partial p_f/\partial x}{2\eta_f} (h_p + L_y) \right] (y - L_y), \tag{2.3}$$

where  $h_f = L_y - h_p$  is the height of the clear fluid layer.

- (iii) The fluid flux,  $q_{f,exp}$ , is written as

$$q_{f,exp} = \int_0^{h_p} (1 - \phi)u_p \, dy + \underbrace{\int_{h_p}^{L_y} u_f \, dy}_{q_f}, \tag{2.4}$$

considering that the fluid velocity matches the particle velocity inside the bed.

Using the experimental flow rate per unit width,  $q_{f,exp}$ , and the experimental vertical profiles of  $\phi$  and  $u_p$ , the pure fluid flow rate  $q_f$  is deduced from (2.4) by numerical integration and the pressure gradient for the parabolic velocity profile is then obtained as  $\partial p_f / \partial x = (6\eta_f / h_f^3)(h_f u_{p,in} - 2q_f)$ . Inserting this value in (2.3), we can calculate the fluid velocity profile in the pure fluid zone, see the black full curves in figure 1(b–d). The agreement with the experimental fluid velocity measurement for the PMMA particles is found to be good, see figure 1(d). This validates the present reconstruction method and its use for the borosilicate particles. Note that this method does not enforce a continuity of stress from the clear fluid phase to the particle phase; the obtained fluid and particle velocity profiles exhibit a change in slope at the fluid/bed interface. The fluid shear stress at the bed interface is then given by  $\tau_f(h_p) = \frac{1}{2}(\partial p_f / \partial x)(L_y - h_p) - \eta_f u_{p,in} / h_f$  and the vertical profile of the shear rate is simply given by (2.1).

The extraction and reconstruction methods described above provide all the quantities needed to investigate the rheology of the mobile sediment bed:  $\mu(J)$  and  $\phi(J)$  or equivalently  $\eta_s(\phi)$  and  $\eta_n(\phi)$ .

### 3. Simulation data

In the present work, we use the framework described in detail in Biegert *et al.* (2017a,b) to execute several simulations in an attempt to compare to the different experimental results of Aussillous *et al.* (2013) at different flow rates and fluid heights. In order to keep the paper self-contained, we provide a brief summary of the computational approach.

The particle-laden flows of interest require us to solve the Navier–Stokes equation

$$\rho_f \left[ \frac{\partial \mathbf{u}_f}{\partial t} + \nabla \cdot (\mathbf{u}_f \mathbf{u}_f) \right] = \nabla \tau_f + \mathbf{f}_b + \mathbf{f}_{IBM}, \tag{3.1}$$

where  $\mathbf{u}_f = (u_f, v_f, w_f)^T$  denotes the fluid velocity vector and  $t$  time. The fluid stress tensor is given by  $\tau_f = -p_f \mathbf{E} + \eta_f [\nabla \mathbf{u}_f + (\nabla \mathbf{u}_f)^T]$ , where  $p_f$  represents the fluid pressure with the hydrostatic component subtracted out and  $\mathbf{E}$  the identity matrix. The right-hand side includes the volume forces  $\mathbf{f}_b = (f_{b,x}, 0, 0)^T$  and  $\mathbf{f}_{IBM}$ . The former is a source term used to create the pressure gradient driving the flow and the latter an immersed boundary force used to enforce the no-slip condition on the particle surface. We discretise the equations of motion for the fluid on a cubic finite difference mesh ( $\lambda = \Delta x = \Delta y = \Delta z$ ).

The numerical treatment is based on the IBM for fluid–particle coupling (Uhlmann 2005; Kempe & Fröhlich 2012a) and the scheme of Biegert *et al.* (2017a) for particle–particle interaction.

We solve for the translational velocity,  $\mathbf{u}_p$ ,

$$m_p \frac{d\mathbf{u}_p}{dt} = \underbrace{\oint_{\Gamma_p} \tau_f \cdot \mathbf{n} \, dA}_{=F_{h,p}} + \underbrace{V_p (\rho_p - \rho_f) \mathbf{g}}_{=F_{g,p}} + \mathbf{F}_{i,p}, \tag{3.2}$$

and the angular velocity,  $\boldsymbol{\omega}_p$ ,

$$I_p \frac{d\boldsymbol{\omega}_p}{dt} = \underbrace{\oint_{\Gamma_p} \mathbf{r}_p \times (\tau_f \cdot \mathbf{n}) \, dA}_{=T_{h,p}} + \mathbf{T}_{i,p}, \tag{3.3}$$

of spherical particles, where  $m_p$  is the particle mass,  $I_p$  the particle moment of inertia,  $V_p$  the particle volume and  $\mathbf{g} = (0, -g, 0)^T$  the gravitational acceleration vector. The fluid



acts on the particles through the hydrodynamic stress tensor  $\boldsymbol{\tau}_f$ , where  $\mathbf{r}_p$  represents the vector from the particle centre to a point on the surface  $\Gamma_p$  and  $\mathbf{n}$  is the unit normal vector pointing outwards from that point. The net force and torque acting on the particle centre of mass due to particle interactions are given by  $\mathbf{F}_{i,p}$  and  $\mathbf{T}_{i,p}$ , respectively.

We evaluate the particle interaction forces and torques according to Biegert *et al.* (2017a). The resulting collision model involves normal contact forces,  $\mathbf{F}_n$ , tangential (frictional) contact forces,  $\mathbf{F}_t$ , and short-range hydrodynamic lubrication forces,  $\mathbf{F}_l$ , to provide the total collision force

$$\mathbf{F}_{i,p} = \sum_{q, q \neq p}^{N_{tot}} (\mathbf{F}_{l,pq} + \mathbf{F}_{n,pq} + \mathbf{F}_{t,pq}), \quad (3.4)$$

where  $N_{tot}$  is the total number of particles and the subscript  $pq$  indicates interactions of particle  $p$  with particle  $q$ . According to Cox & Brenner (1967), we model the unresolved hydrodynamic component of the lubrication forces in our simulations as

$$\mathbf{F}_{l,pq} = \begin{cases} -\frac{6\pi\eta_f R_{eff}^2}{\max(\zeta_n, \zeta_{min})} \mathbf{g}_n & 0 < \zeta_n \leq 2h \\ 0 & \text{otherwise} \end{cases} \quad (3.5)$$

where  $\zeta_n$  is the gap size,  $R_{eff} = R_p R_q / (R_p + R_q)$  the effective radius and  $R_p$  and  $R_q$  are the radii of the two interacting particles. Furthermore,  $\zeta_{min} = 3 \times 10^{-3} R_p$  is a limiter as calibrated by Biegert *et al.* (2017a) that can be interpreted as the roughness of the particle surface and  $\mathbf{g}_n$  is the normal component of the relative velocity of the two colliding particles. The repulsive normal component is represented by a nonlinear spring-dashpot model for the normal direction

$$\mathbf{F}_{n,pq} = -k_n |\zeta_n|^{3/2} \mathbf{n} - d_n \mathbf{g}_n, \quad (3.6)$$

where  $k_n$  and  $d_n$  represent stiffness and damping coefficients that are adaptively calibrated for every collision/contact to prescribe a restitution coefficient of  $e_{dry} = -u_o/u_i = 0.97$  (Kempe & Fröhlich 2012b). Here,  $u_o$  and  $u_i$  indicate the normal components of the relative particle speed immediately after and right before the particle contact, i.e.  $\zeta_n = 0$ . The forces in the tangential direction are modelled by a linear spring-dashpot system capped by the Coulomb friction law as

$$\mathbf{F}_{t,pq} = \min(-k_t \boldsymbol{\zeta}_t - d_t \mathbf{g}_{t,cp}, \|\mu_f \mathbf{F}_n\| \mathbf{t}), \quad (3.7)$$

where  $k_t$  and  $d_t$  are stiffness and damping computed according to Thornton, Cummins & Cleary (2011) and Thornton, Cummins & Cleary (2013),  $\mu_f = 0.15$  represents the friction coefficient between the two surfaces,  $\boldsymbol{\zeta}_t$  is the tangential displacement integrated over the time interval for which the two particles are in contact (Thornton *et al.* 2013) and  $\mathbf{t}$  is a unit vector pointing into the tangential direction. The empirical parameters  $e_{dry} = 0.97$  and  $\mu_f = 0.15$  have been taken from experiments involving glass spheres (Gondret, Lance & Petit 2002; Joseph & Hunt 2004). Using these values, the contact model has been validated in detail by Biegert *et al.* (2017a) against seminal experimental benchmark data involving the same material (Foerster *et al.* 1994; Gondret *et al.* 2002; Ten Cate *et al.* 2004; Aussillous *et al.* 2013). Note that these parameters were not measured for the particles used in the experiments of Aussillous *et al.* (2013) and may, hence, be different.

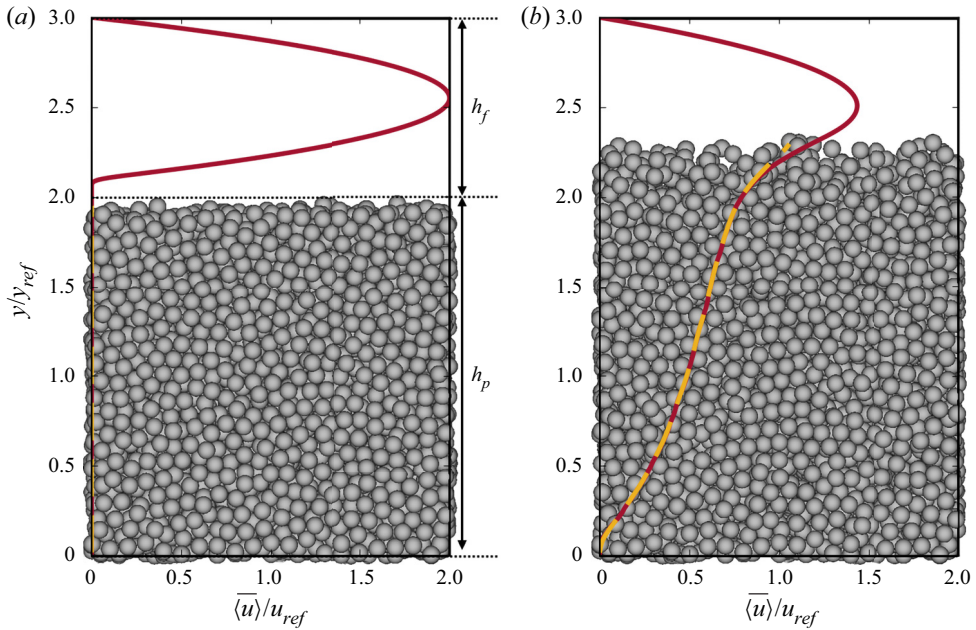


Figure 2. (a) Initial conditions for fluid velocity and bed configuration at  $t/t_{base} = 0$  and (b) fully developed state at  $t/t_{base} = 10$  for simulation Re67 as listed in table 2. Lines indicate the average streamwise ( $x$ -direction) fluid velocity (dark grey, red online) and particle velocity (light grey, yellow online), where the consecutive averaging in the horizontal plane and time is defined by (3.9).

In the present work, we consider a computational set-up very similar to the one presented in Aussillous *et al.* (2013) (figure 2a). The domain has dimensions  $L_x \times L_y \times L_z = 20d_p \times 30d_p \times 10d_p$ . We discretise the domain with a regular grid that is equidistant in all three directions and has a resolution of 25.6 grid cells per particle diameter, which is a fine enough resolution to obtain results independent of the grid cell size, as shown by Biegert *et al.* (2018). We generate the bed by allowing 4339 monodisperse particles to settle under gravity, without the influence of the surrounding fluid, onto a layer of 200 fixed particles whose centres randomly vary in height above the bottom wall within a range of  $d_p$ , providing an irregular roughness (Jain, Vowinckel & Frhlich 2017). The resulting bed fills the domain to approximately a height of  $h_p \approx 20d_p$  from the bottom wall, where  $h_p$  is the particle bed height, leaving a gap of approximately  $10d_p$  between the top wall and the top of the particle bed. For the simulation runs, we use a particle density  $\rho_p/\rho_f = 2.1$  and a Galileo number of  $Ga = 0.85$ . A definition of  $Ga$  as well as a summary of the relevant simulation parameters is given in table 1. We employ a predefined Poiseuille flow in the clear fluid region above the sediment bed as a reference case for the simulation. For this reference case, we define the reference length  $y_{ref} = 10d_p = L_y/3$ , the reference velocity of  $u_{ref} = -y_{ref}^2 f_{b,x}/(12\eta_f)$  and the reference stress  $\sigma_{ref} = -y_{ref} f_{b,x}/2$  to compute the corresponding Reynolds and Shields numbers (cf. table 2).

We enforce different volumetric flow rates, governed by the volume force  $f_{b,x}$ . As it can take a long time for a simulation to reach a statistically steady state when initialised from rest, we found it to be more efficient to obtain a steady state by initialising the flow with a large pressure gradient that mobilises the entire bed (run Re67 in figure 3(a) and table 2). To allow for a direct comparison among the different runs, we therefore

Number of particles $N_{tot}$	4339
Galileo number $Ga = \frac{\rho_f}{\eta_f} \sqrt{\left(\frac{\rho_p}{\rho_f} - 1\right) g d_p^3}$	0.85
$\rho_p/\rho_f$	2.1
Timestep	CFL = 0.5
Domain size ( $L_x/d_p \times L_y/d_p \times L_z/d_p$ )	$20 \times 30 \times 10$
Domain grid size ( $L_x/\lambda \times L_y/\lambda \times L_z/\lambda$ )	$512 \times 768 \times 256$
Domain boundary conditions	periodic $\times$ no-slip $\times$ periodic
Initial $h_f/d_p$	10.0
Particle resolution, $d_p/\lambda$	25.6

Table 1. Simulation parameters for the pressure-driven flow over a bed of particles. CFL, Courant–Friedrichs–Lewy.

Simulation run	$Re_{ref}$	$Sh_{ref}$	$t_{sim}/t_{base}$	$t_{avg}/t_{base}$
Re67	66.7	11.1	[0.00, 10.00]	initialisation
Re17	16.7	5.53	[10.00, 47.20]	[16.00, 47.20]
Re33	33.3	2.77	[10.00, 58.80]	[44.00, 52.15]
Re8	8.33	1.38	[47.20, 92.05]	[77.00, 92.05]

Table 2. Simulation parameters for different runs of the pressure-driven flow over a bed of particles. The Reynolds and Shields numbers based on the reference case (predefined Poiseuille flow above the sediment bed), i.e.  $Re_{ref} = \rho_f u_{ref} y_{ref} / \eta_f$  and  $Sh_{ref} = \sigma_{ref} / [(\rho_p - \rho_f) g d_p]$ , respectively. The individual simulation is run for the duration  $t_{sim}$ , and the momentum balance is analysed by using time-averaged data over the interval  $t_{avg}$ .

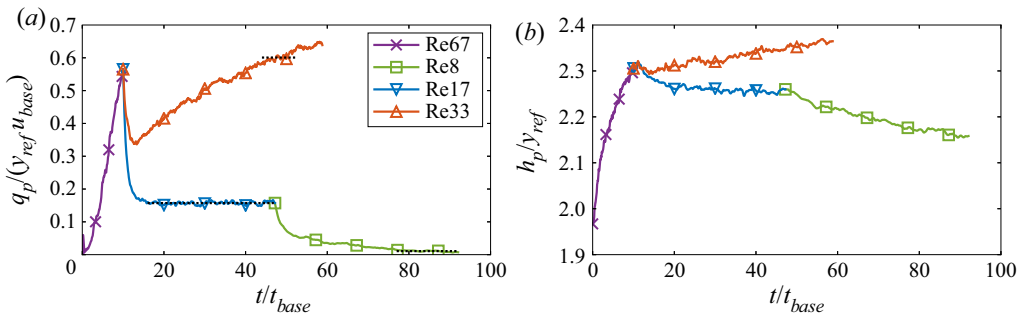


Figure 3. Sheared particle bed. (a) Particle volumetric flux  $q_p = (1/L_x L_z) \sum_{p=1}^{N_{tot}} V_p u_{p,x}$ , for the different simulation runs. Dotted lines indicate the average particle flux over the averaging time interval for each simulation. (b) Bed height, defined at  $\langle \phi \rangle = 0.05$ .

define  $u_{base} = u_{ref}$  (Re67),  $t_{base} = y_{ref} / (1.5u_{base})$  and  $\sigma_{base} = \sigma_{ref}$  (Re67). By the end of the simulation Re67, the bed has dilated to a height of  $h_p/y_{ref} \approx 2.3$  (figure 3b), and the particles just above the fixed layer at the bottom of the domain are moving (figure 2b). After this initialisation phase, the imposed pressure gradient is reduced to produce simulations Re17 and Re33. Re8 is carried out by continuing Re17 with an even lower imposed pressure gradient. This procedure allows us to quickly reach a steady state for runs Re17 and Re8, as can be seen in figure 3(a), whereas Re33 is still in the process of dilation.

To compare the simulation results to rheological models, we have to analyse the discrete information of the particle phase in our simulations, such as particle velocities and forces,

from a continuum viewpoint. To this end, we employ the coarse-graining method (CGM) based on the works of Goldhirsch (2010) and Weinhart *et al.* (2012). This CGM conserves quantities of interest, but additionally smooths out the resulting continuum field. For a given discrete particle quantity  $\theta_p$ , we define its coarse-grained continuous counterpart,  $\theta^{cg}$ , as

$$\theta^{cg}(\mathbf{x}, t) = \sum_{p=1}^{N_{tot}} \theta_p \mathcal{W}(\mathbf{x} - \mathbf{x}_p(t)), \quad (3.8)$$

where  $\mathbf{x}_p(t)$  is the position of the centre of particle  $p$ , and  $\mathcal{W}(r)$  is the conservative coarse-graining function that smears a given local quantity in a spherical volume of radius  $|r|$ . The main property is that  $\int_{\mathbb{R}^3} \mathcal{W}(r) \, d\mathbf{r} = 1$ . We implemented a coarse-graining function based on the Dirac delta function of Roma, Peskin & Berger (1999), which is the same delta function used in the IBM (Uhlmann 2005). The filter  $|r|$  has to be as small as possible to fully exploit the highly resolved simulation data for our rheological analysis, but large enough to smooth out the sub-particle scale. Here, we choose  $|r| = 1.5d_p$ , which was deemed to be a good compromise to satisfy these requirements.

The steady-state configuration for the moving bed is steady only in a time-averaged sense, because particle collisions and positions continuously fluctuate. We therefore define the time average of a given continuous field  $\theta$  to be

$$\overline{\langle \theta \rangle}(y) = \frac{1}{t_{avg,2} - t_{avg,1}} \int_{t_{avg,1}}^{t_{avg,2}} \frac{1}{L_x L_z} \int_0^{L_z} \int_0^{L_x} \theta(x, y, z, t) \, dx \, dz \, dt, \quad (3.9)$$

where the overbar and angular brackets represent averaging in time and space, respectively (Vowinckel, Kempe & Fröhlich 2014; Vowinckel *et al.* 2017a,b). Note that this averaging operator applies for both continuous fluid quantities and coarse-grained particle quantities. We present the values for  $t_{avg,1}$  and  $t_{avg,2}$  in table 2. These time-averaging windows were chosen to capture the steady-state results, or as large a time span as possible for as similar a particle flux as possible (figure 3). We will show, however, that our results for the rheology are independent of transient behaviour for all Reynolds numbers investigated.

We can use (3.8) to obtain a continuous field of  $\phi$  and (3.9) to generate vertical profiles of  $\overline{\langle \phi \rangle}$  and  $\overline{\langle u_f \rangle}$  by computing double-averaged values (in space and time, cf. figure 4). For the analysis of the rheology, we exclude values for  $y/y_{ref} < 0.68$  to eliminate boundary effects from the artificial bed roughness at the bottom wall. We observe the same evolution for the volume fraction as in the experiments with a rapid increase downward from the fluid–particle interface to reach a constant value after a few sphere diameters. Here, we follow the definition of Biegert *et al.* (2017a) to determine the fluid–sediment interface at  $\overline{\langle \phi \rangle} = 0.05$ . The oscillations of  $\overline{\langle \phi \rangle}$  in this region reflect the sub-particle scale as the particle are layered within the sediment bed (figure 4a). We therefore apply the coarse-graining radius of  $|r| = 1.5d_p$  to the grid resolved data shown in this figure to smooth out the layered structure in these vertical profiles. Note that figure 4(b) yields  $\dot{\gamma} = \partial \overline{\langle u_f \rangle} / \partial y$  as another rheological quantity. Looking at the double-averaged fluid velocity profiles in figure 4(b), the three cases represent three distinctively different regimes (Jenkins & Larcher 2017). The sediment bed of Re8 reaches a quasi-static regime of the granular suspension, whereas the sediment motion in Re17 and Re33 can be considered ‘layered’ and ‘collisional’, respectively. There is a clear qualitative difference between run Re8, whose velocity profile is concave and goes to zero within the bed at  $y/y_{ref} \approx 0.5$ , and run Re33, whose velocity profile is convex, goes to zero only at the fixed particles at

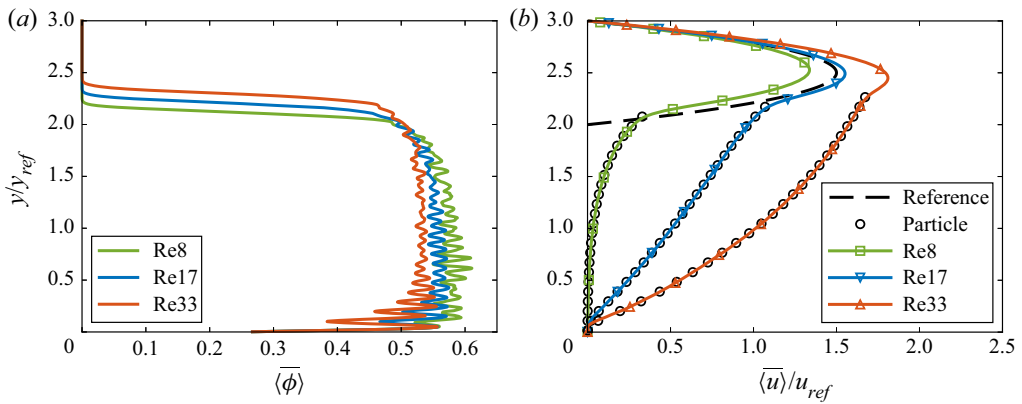


Figure 4. Sheared particle bed: profiles for the different simulation runs averaged horizontally and in time for (a) the particle volume fraction and (b) the streamwise velocity. The average fluid velocity (solid coloured lines) is given by (3.9), while the average coarse-grained particle velocity (circles) is given by (3.8).

the lower wall. Note that the fluid velocity is to a good approximation equal to the particle velocity, which is consistent with the observation of Aussillous *et al.* (2013). The Stokes number is in the range  $0.19 \leq St \leq 0.77$ , which is 20 to 80 times larger than the values obtained from the experimental data § 2, but still expected to be in the viscous regime (Ness & Sun 2015).

While we can readily extract the quantities for  $\phi$  and  $\dot{\gamma}$  from figure 4, an additional investigation of the total stress balance of the fluid–particle mixture in  $x$ - and  $y$ -directions is needed to compute the total shear stress  $\tau$  and the granular pressure  $p_p$  as will be detailed in the next section.

#### 4. Stress balance of the simulation data

This section presents the analysis of the stress balance for the fluid–particle mixture to compute wall-normal profiles of the rheological quantities  $\tau$  and  $p_p$ . To this end, we follow the argument of the previous numerical work (Biegert 2018; Biegert *et al.* 2018; Vowinckel *et al.* 2019), where the full derivation of the stress balances in both shearing ( $x$ ) and wall-normal ( $y$ ) directions is given from first principles. In addition, a detailed analysis of the present data sets for all components entering the stress balances in the shear and wall-normal directions can be found in Biegert (2018).

##### 4.1. Stress balance in the $x$ -direction to obtain the total stress

To obtain the total shear stress, we consider the momentum balance of the fluid phase, i.e. the Navier–Stokes equations (3.1), over the control volume  $\Omega_{CV}$  in the  $x$ -direction spanning from the top wall  $\Gamma_w$  to some arbitrary height  $y$  with the lower boundary being  $\Gamma_y$  and involving multiple particles (figure 5). We distinguish the free fluid from the particle interior as exemplified in figure 5 using  $\Omega_{CV}^+$  and  $\Gamma_y^+$  for parts of the domain that are occupied by fluid and the lower boundary, respectively.

We can simplify the momentum balance of the fluid phase for the following reasons. Owing to the periodic boundary conditions and the fact that we impose the Poiseuille flow via the volume force  $f_b$ , the pressure term ( $\partial p_f / \partial x$  in (3.1)) does not contribute to the  $x$ -momentum, since our control volume covers the entire streamwise extent of the domain.



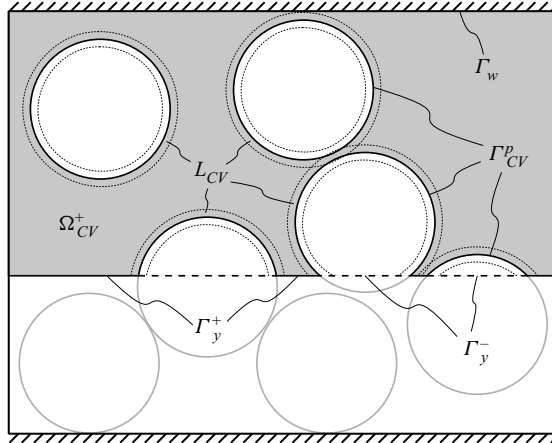


Figure 5. Shaded control volume for the averaging involving multiple particles. All of the volumes and surfaces required for (4.1) are indicated.

At the top wall  $\Gamma_w$ , the vertical velocity,  $v_f$ , is zero, so that only  $\eta_f \partial u_f / \partial y$  contributes to the fluid stress. At the lower boundary,  $\Gamma_y$ , the pressure again does not play a role and the convective term vanishes due to the laminar flow conditions, so that the long-range hydrodynamic stress originates from the viscous term. Finally, we include  $f_{IBM,x}$  as the sum of all hydrodynamic stresses arising from pressure and viscous forces that act on the particle surfaces  $L_{CV}$  enclosed in  $\Omega_{CV}$ . These assumptions yield

$$\underbrace{\int_{\Gamma_w} \eta_f \frac{\partial u_f}{\partial y} dA + \int_{\Omega_{CV}} f_{b,x} dV}_{\text{External force}} = \underbrace{\int_{\Gamma_y^+} \eta_f \left( \frac{\partial u_f}{\partial y} + \frac{\partial v_f}{\partial x} \right) dA}_{\text{Fluid force}} - \underbrace{\int_{L_{CV}} f_{IBM,x} dV}_{\text{Particle force}}. \tag{4.1}$$

The last term Particle force provides the linkage to the momentum balance of the particle phase, which can be obtained by applying the CGM (3.8) to the particle equation of motion (3.2). This yields

$$\mathbf{a}^{cg} = \mathbf{F}_h^{cg} + \mathbf{F}_g^{cg} + \mathbf{F}_i^{cg}, \tag{4.2}$$

where  $\mathbf{a}^{cg}$ ,  $\mathbf{F}_h^{cg}$ ,  $\mathbf{F}_g^{cg}$  and  $\mathbf{F}_i^{cg}$  are the coarse-grained forces due to the particle acceleration, hydrodynamic stress due to the IBM, gravity and particle interactions, respectively. Similar to the fluid momentum balance, we can analyse the coarse-grained particle forces within a control volume spanning the entire domain in the streamwise and spanwise directions and extending from the top wall to an arbitrary height  $y$ . Integrating (4.2) over this volume, we obtain

$$\int_{\Omega_{CV}} \mathbf{a}^{cg} dV = \int_{\Omega_{CV}} \left( \mathbf{F}_h^{cg} + \mathbf{F}_g^{cg} + \mathbf{F}_i^{cg} \right) dV. \tag{4.3}$$

If particles are in a steady state, either naturally or through double averaging, then the acceleration term vanishes. Furthermore, our set-up of a horizontal channel yields  $F_{g,x} = 0$ . We can, therefore, use the fact that  $f_{IBM,x} = F_{h,x}^{cg} = -F_{i,x}^{cg}$  and apply (3.4)

to further distinguish between normal and tangential forces due to particle contact and friction ( $F_{n,x}^{cg}$  and  $F_{t,x}^{cg}$ ) and short-range hydrodynamic lubrication forces ( $F_{l,x}^{cg}$ ).

Using the averaging operator (3.9) and dividing by the horizontal area of the domain, we can rewrite (4.1) as

$$\underbrace{\eta_f \left\langle \frac{\partial u_f}{\partial y} \Big|_{L_y} \right\rangle + \bar{f}_{b,x}(L_y - y)}_{\text{External/total stress}} = \underbrace{\eta_f \left\langle \gamma \left( \frac{\partial u_f}{\partial y} + \frac{\partial v_f}{\partial x} \right) \Big|_y \right\rangle - \int_y^{L_y} \overline{\langle F_{l,x}^{cg} \rangle} dy}_{\text{Hydrodynamic stress}} + \underbrace{\int_y^{L_y} \left( \overline{\langle F_{n,x} \rangle} + \overline{\langle F_{t,x} \rangle} \right) dy}_{\text{Contact stress}}, \quad (4.4)$$

where  $\gamma$  is an indicator function for the fluid ( $\gamma = 1$  outside the particle and  $\gamma = 0$  inside the particle), resulting in double-averaged equations for laminar flows akin to Nikora *et al.* (2013) and Vowinckel *et al.* (2017a,b). We have also used the fact that  $\eta_f$ ,  $\rho_f$  and  $\bar{f}_{b,x}$  are constant throughout the domain. It is important to note that we are explicitly separating the stresses arising from hydrodynamic interactions and particle contacts, respectively (Gallier *et al.* 2014; Gallier, Peters & Lobry 2018), which will be analysed in more detail in § 5. The right-hand side of (4.4) comprises the long-range fluid stress due to viscous effects evaluated at height  $y$  at the boundaries of the control volumes  $\Gamma_{CV}^+$  occupied by fluid as well as the short-range lubrication effects within the control volume  $\Gamma_{CV}^+$ . The contact stress comprises both, normal contact forces and tangential frictional forces. Note that it was shown in Biegert *et al.* (2018) and Biegert (2018) that there is also a viscous and convective stress inside the particles  $\Gamma_{CV}^-$  as a by-product of the IBM. For the present study, this effect does not contribute a significant part to the total stress balance. The external stress on the left-hand side of (4.4) consists of the viscous stress at the top wall and the stress from the body force acting throughout the control volume. It is also equal to all other stresses arising from the movement of the fluid and particles and is hence equivalent to the total stress  $\tau_f$  needed to compute the rheological quantities  $\mu(J)$  and  $\eta_s$ .

For the analysis of the stress balance of the fluid phase, we focus on runs Re8 and Re33 to get a sense of the results for different flow conditions. Figure 6 shows the momentum balance of the fluid phase, given by (4.4), for runs Re8 (figure 6a) and Re33 (figure 6b), in which we expect the external stress to match the sum of the hydrodynamic and contact stresses. As expected, the external stress at the top wall is close to  $\overline{\langle \sigma_x \rangle} / \sigma_{ref} = -1$ . In the upper part of the flow ( $y/y_{ref} > 2.15$  and  $y/y_{ref} > 2.3$  for Re8 and Re33, respectively), there are no particles, and the hydrodynamic stress matches all of the external stress. Within the particle bed ( $y/y_{ref} < 2.3$ ), however, the majority of the external stress is taken up by particle contact. The total stress comes out to be a linear profile. Hence, the present results support the conceptual model (2.1) proposed by Aussillous *et al.* (2013) (figure 4(b) in this reference) and we can use these data to compute  $\eta_s$  and  $\mu$  in the following.

Naturally, the hydrodynamic stress of the laminar flow is entirely made up of the viscous term alone. Run Re8 differs from Re33 in that the hydrodynamic stress reaches a higher positive value above the particle bed and quickly drops to zero within the particle bed. The hydrodynamic stress for Re33, on the other hand, increases with increasing depth within the particle bed. Since the entire sediment bed is set in motion for this case, the lubrication component makes a significant contribution to the hydrodynamic stress. These results are consistent with the velocity profiles in figure 4(b), where the concavity of the profile for Re8 results in a high shear stress at the fluid/particle bed interface and low stresses

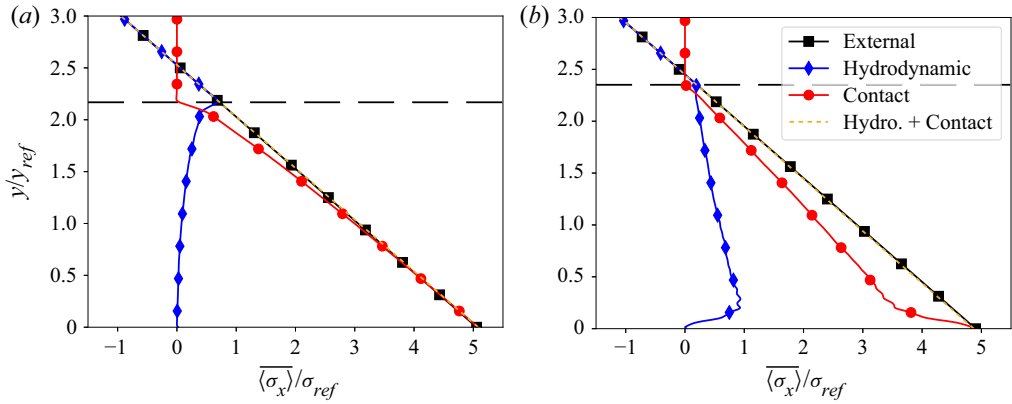


Figure 6. Stress balance of the fluid phase in the  $x$ -direction for a sheared particle bed according to (4.4). (a) run Re8 and (b) run Re33. The horizontal dashed line marks the height of the particle bed,  $h_p$ . As shown in (a,b), the sum of the hydrodynamic and contact stresses is in equilibrium with the external stress and consists mostly of the contact stress within the bed and the hydrodynamic stress above the bed.

within the bed, while the convexity of the profile for Re33 leads to a large shear stress at the lower wall. The total stress, on the other hand, is completely dominated by particle contact within the sediment bed. This result is consistent with the locations of the sharp gradients in the stress balance, so that the hydrodynamic and contact stresses together close the  $x$ -momentum balance. It also shows that effects from the local acceleration term are negligible and that the unsteady flow conditions (figure 3) are expected to have no impact on the reported results even for cases of dilating and consolidating sediment beds (e.g. Re33).

#### 4.2. Stress balance in the $y$ -direction to obtain particle pressure

The rheological quantities  $\eta_n$  and  $\mu(J)$  require information about the particle pressure  $p_p$ , which we can obtain by further analysing the particle phase. Another way to interpret the bed particle pressure  $p_p$  is to think of it as the total submerged weight of the particles (Vowinckel *et al.* 2019). Indeed, this has been done by Stickel & Powell (2005) and Ouriemi *et al.* (2009) for continuum modelling. We can demonstrate the validity of this reasoning by analysing the momentum balance for the particle phase in the  $y$ -direction. To this end, we utilise the coarse-grained momentum balance of the particle phase (4.2) and apply the averaging operator (3.9) to recast (4.3) as a line integral in the wall-normal direction

$$\int_y^{L_y} \overline{\langle a^{cg} \rangle} dy = \int_y^{L_y} \left( \overline{\langle F_h^{cg} \rangle} + \overline{\langle F_g^{cg} \rangle} + \overline{\langle F_i^{cg} \rangle} \right) dy. \tag{4.5}$$

Since we are interested in the granular pressure, i.e. the bed weight, we consider only the vertical  $y$ -component. We again neglect the acceleration term, but keep the gravity term that is acting in the same vertical direction. Furthermore, we subdivide  $F_i^{cg}$  into the short-range hydrodynamic lubrication and particle contact component,  $F_l^{cg}$  and  $F_n^{cg}$  and

$F_t^{cg}$ , respectively,

$$\begin{aligned}
 - \underbrace{\int_y^{L_y} \overline{\langle F_{g,y}^{cg} \rangle} dy}_{\text{Bed weight}} &= \underbrace{\int_y^{L_y} \overline{\langle F_{h,y}^{cg} \rangle} dy + \int_y^{L_y} \overline{\langle F_{l,y}^{cg} \rangle} dy}_{\text{Hydrodynamic stress}} \\
 &+ \underbrace{\int_y^{L_y} \overline{\langle F_{n,y}^{cg} \rangle} dy + \int_y^{L_y} \overline{\langle F_{t,y}^{cg} \rangle} dy}_{\text{Contact stress}}. \tag{4.6}
 \end{aligned}$$

Since  $F_{g,p} = V_p(\rho_p - \rho_f)\mathbf{g}$ , coarse graining the particle weight yields the left-hand side as the submerged bed weight, which is equivalent to the particle pressure

$$p_p = (\rho_p - \rho_f)|\mathbf{g}| \int_y^{L_y} \overline{\langle \phi \rangle} dy. \tag{4.7}$$

We also note that (4.7) is the integral of (2.2), so that the present derivation provides a direct linkage to the two-phase modelling of Aussillous *et al.* (2013). Owing to the fact that we obtain full information of the solid volume fraction (cf. figure 4b), we do not need to introduce an artificial pressure at the fluid sediment interface. This was suggested by Houssais *et al.* (2016) (called  $P_0$  in that study), but using such an artificial pressure would neither be in line with the two-phase modelling, nor would it obey the definition of our control volume sketched in figure 5. Hence, omitting  $P_0$  naturally yields  $J \rightarrow \infty$  for  $\phi \rightarrow 0$ , because  $p_p \rightarrow 0$ . This behaviour is consistent with the approach of Boyer *et al.* (2011).

Figure 7 shows the coarse-grained particle phase stresses, given by the time average of (4.6) for runs Re8 (a) and Re33 (b). In figures 7(a) and 7(b), the bed weight increases almost linearly from the top of the particle bed down to the lower wall, balanced by the sum of the hydrodynamic and collision stresses. Again, this observation confirms the conceptual model of (2.2) of Aussillous *et al.* (2013). The fact that we have found a linear profile for this physical quantity simplifies the situation from a modelling perspective, i.e. one needs the sediment height and the total submerged weight of the sediment bed to reconstruct depth-resolved profiles of  $p_p$ . The results for the stress balance in  $y$ -direction show clear differences between runs Re8 and Re33. Owing to the normalisation, the dimensionless  $y$ -momentum collision stress is three times larger for Re8 than for Re33. Moreover, the hydrodynamic stress is positive for Re8 and negative for Re33, so that the collision stresses are less than and greater than the bed weight, respectively, for the stress balance to be in equilibrium. These deviations from zero stem from the fact that Re8 and Re33 are in the process of consolidation and dilation, respectively.

### 5. Rheology

We now turn to the examination of the rheological quantities extracted from the experimental measurements in § 2 and from the numerical simulations in §§ 3 and 4. We display these data within the pressure-imposed view by plotting the effective friction coefficient,  $\mu = \tau/p_p$ , and the bulk volume fraction,  $\phi$ , as a function of the viscous number,  $J = \eta_f \dot{\gamma}/p_p$ , in figure 8. The macroscopic friction coefficient,  $\mu$ , is found to be an increasing function of the viscous number,  $J$ , whereas the volume fraction,  $\phi$ , is a decreasing function of the viscous number,  $J$ , for both the experimental data coming from the two batches of spheres made of borosilicate (+) and PMMA (x), where no appreciable

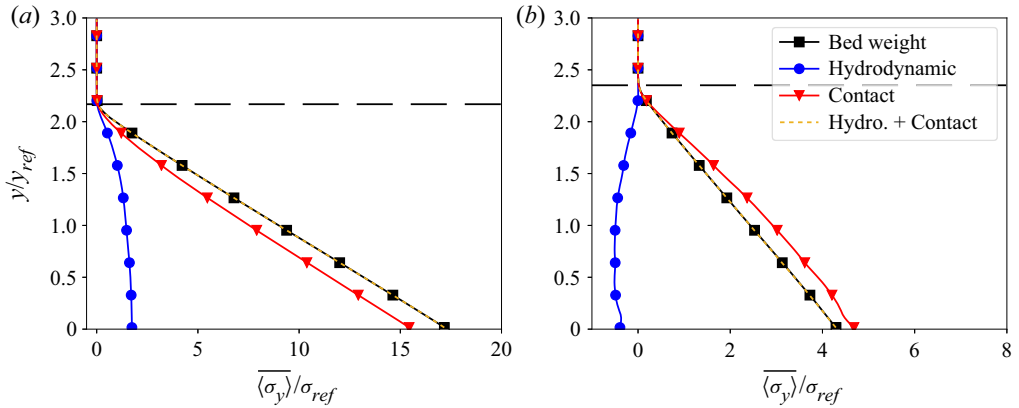


Figure 7. Stress balance of the particle phase in the  $y$ -direction for sheared particle beds according to (4.6). (a) run Re8 and (b) run Re33. The horizontal dashed line marks the height of the particle bed,  $h_p$ . Panels (a,b) show that the sum of the hydrodynamic and contact stresses is in equilibrium with the bed weight, i.e.  $p_p$ , with most of the weight supported by the contact stress. The hydrodynamic lift force acting on the particles can be (a) positive or (b) negative.

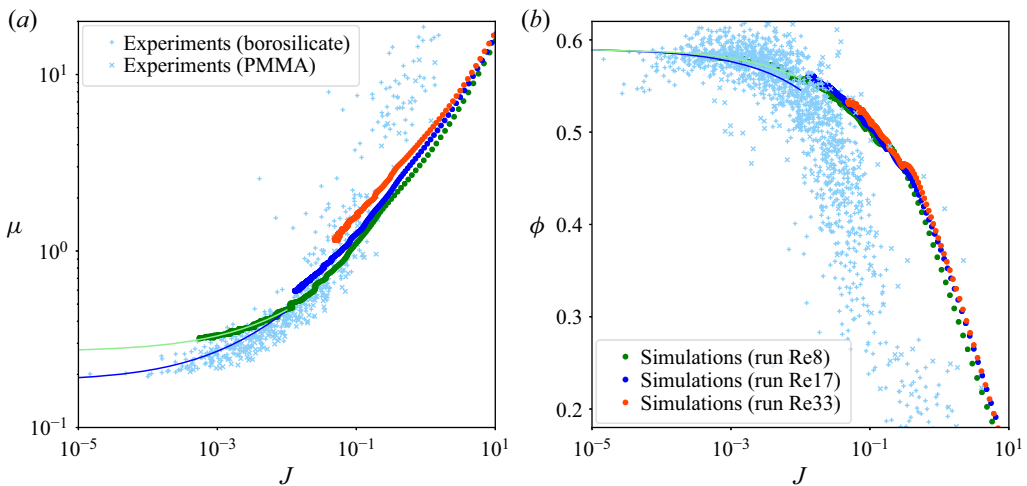


Figure 8. (a) Effective friction coefficient,  $\mu = \tau / p_p$ , and (b) bulk volume fraction,  $\phi$ , vs the viscous number,  $J = \eta_f \dot{\gamma} / p_p$ . The solid lines are the asymptotic linear regressions in  $\sqrt{J}$  (blue for the experiments and green for the simulations).

differences can be seen between the runs of these two particle materials, and the numerical data coming from the three different runs at different Reynolds numbers.

It is important to note, however, that figure 8 is not meant as a validation of the numerical results by comparing it to the post-processed experimental data of Aussillous *et al.* (2013) for the following reasons. First, the two data sets represent different conditions. The particle properties  $e_{dry}$  and  $\mu_f$  chosen for the simulations may not correspond to the (unknown) values of the experiments and the flow conditions expressed by the Stokes number differ by more than one order of magnitude. Second, owing to the difficulty in capturing experimentally the sediment transport layer close to the bed interface of only a few particle diameters thickness, the experimental data present significant scatter.



Finally, recall that our data processing in § 2 assumes  $u_f = u_{p,in}$  to reconstruct the experimental velocity profile, which slightly underestimates the fluid velocity in the sediment transport layer. On a similar note, the averaging operator using coarse-grained quantities (3.8) for the simulations yields an averaging window of three diameters in height to smooth out the sub-particle scale. For all these reasons, we can observe a rather large discrepancy between the experimental and numerical data for large  $J$ , i.e. in the sediment transport layer, but the qualitative trend is correctly reproduced.

Despite the discrepancy at large  $J$ , both data sets show asymptotic behaviour for small  $J$  in figure 8(b). The results can therefore be used to deduce the critical parameters  $\mu_c$  and  $\phi_c$  and provide proper scaling for our rheological analysis. Among the numerical results, only the data for the smallest Reynolds number (run Re8) reach the limit of small  $J$ , i.e.  $J < 10^{-2}$  and, hence, small  $\dot{\gamma}$ . The data coming from run Re8 and from the experiments show that both  $\phi$  and  $\mu$  tend to finite measurable values,  $\phi_c$  and  $\mu_c$  respectively, at vanishing  $J$ , i.e. at the jamming point where the suspension ceases to flow. The critical (or maximum flowable) volume fraction,  $\phi_c$ , and friction coefficient,  $\mu_c$ , can be measured by fitting the data using an asymptotic linear regression in  $\sqrt{J}$  for small  $J$  (for  $J < 10^{-2}$ ) as done by Tapia *et al.* (2019). The critical volume fraction is found to be  $\phi_c \approx 0.59$  for both the experiments and simulations and is similar to the value found for suspensions made of spheres having only small surface roughnesses or equivalently having moderate inter-particle sliding friction coefficients (Boyer *et al.* 2011; Dagois-Bohy *et al.* 2015; Tapia *et al.* 2019). The critical friction coefficient is found to be  $\mu_c \approx 0.18$  for the experiments and  $\mu_c \approx 0.27$  for the simulations. These values are smaller than those found previously ( $\mu_c \approx 0.30$ – $0.37$ ) in a pressure-imposed rheometry (Boyer *et al.* 2011; Dagois-Bohy *et al.* 2015; Tapia *et al.* 2019) but are of the same order of magnitude or even slightly larger than that given ( $\mu_c \approx 0.17$ ) by the correlation of Morris & Boulay (1999), which was meant to match experimental results on shear-induced migration.

The critical values  $\phi_c$  and  $\mu_c$  are not universal parameters but depend on particle properties, i.e. the values of  $\phi_c$  and  $\mu_c$  depend on the particle size distribution but also on their surface properties. It is thus convenient to plot the data of figure 8 by scaling  $\phi$  by  $\phi_c$  and  $\mu$  by  $\mu_c$  for a comparison with pressure-imposed rheological measurements (Boyer *et al.* 2011; Dagois-Bohy *et al.* 2015; Tapia *et al.* 2019) and correlations (Morris & Boulay 1999; Boyer *et al.* 2011). These scaled data shown in figure 9 collapse reasonably well onto the same constitutive curves for the small  $J$ -range ( $J \lesssim 10^{-2}$ ) but present discrepancies at larger  $J$ , i.e. low  $\phi$ . However, the discrepancy at low  $\phi$  is not surprising, because the empirical correlations of Boyer *et al.* (2011) and Morris & Boulay (1999) have been derived by fitting to experimental data of volume fractions  $\phi/\phi_c > 0.5$  for neutrally buoyant particles that are homogeneously distributed in a flow cell. In fact, it is worth noting that there even exist some disparities within the pressure-imposed measurements, as while the data of Dagois-Bohy *et al.* (2015) and Tapia *et al.* (2019) are rather similar, they differ from the data of Boyer *et al.* (2011) at large  $J$ . This is reflected in the correlation of Boyer *et al.* (2011), which is designed to agree with the experimental measurements of Boyer *et al.* (2011). This correlation seems to provide a lower bound for the whole collection of data while that of Morris & Boulay (1999) is more like an upper bound for the data of  $\mu(J)$  reported in figure 9(a). The plotted data, therefore, illustrate the range of uncertainty related to the extrapolation of empirical relations. It is important to stress that these two correlations have different critical values:  $\phi_c = 0.585$  and  $\mu_c = 0.32$  for the correlation of Boyer *et al.* (2011) and  $\phi_c = 0.68$  and  $\mu_c = 0.17$  for the correlation of Morris & Boulay (1999). Note that value of  $\phi_c = 0.68$  is rather unrealistic as it exceeds the randomly closed packing fraction.

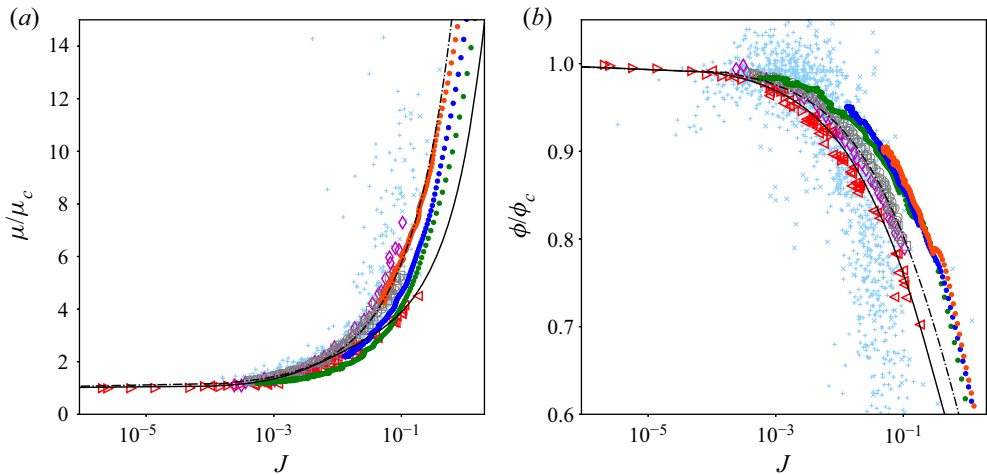


Figure 9. Scaled (a) effective friction coefficient,  $\mu/\mu_c$ , and (b) bulk volume fraction,  $\phi/\phi_c$ , vs the viscous number,  $J = \eta_f \dot{\gamma} / p_p$ . Legend as in figure 8. Comparison with the experiments of Boyer *et al.* (2011) with polystyrene (PS, red  $\blacktriangleleft$ ) spheres of diameter  $d_p = 580 \mu\text{m}$  suspended in polyethylene glycol-ran-propylene glycol monobutylether (PEG) as well as poly(methyl methacrylate) (PMMA, red  $\blacktriangleright$ ) spheres of diameter  $d_p = 1100 \mu\text{m}$  suspended in a Triton X-100/water/zinc chloride mixture, of Dagois-Bohy *et al.* (2015) with PS spheres of similar sizes suspended in PEG (purple  $\diamond$ ), and of Tapia *et al.* (2019) with similar PS spheres which present small roughnesses (SR, grey  $\circ$ ) and with PS spheres which are highly roughened (HR, grey  $\square$ ). Comparison with the correlations proposed by Morris & Boulay (1999) (---) and Boyer *et al.* (2011) (—).

We also provide the classical volume-imposed view by plotting the shear,  $\eta_s = \tau / \eta_f \dot{\gamma} = \mu / J$ , and normal,  $\eta_n = p_p / \eta_f \dot{\gamma} = 1 / J$ , viscosities as a function of the scaled volume fraction,  $\phi / \phi_c$ , in figure 10. The collection of data shows that both viscosities increase with increasing  $\phi$  and diverge at  $\phi_c$ . The data coming from the erosion experiments follow this general trend despite the large scatters. Again, the correlations provide bounds for the whole collection of data of  $\eta_s$  (figure 10a), but this time the correlation of Boyer *et al.* (2011) acts as an upper bound while that of Morris & Boulay (1999) as a lower bound. The simulation data are notably lower than the pressure-imposed rheological measurements of Boyer *et al.* (2011), Dagois-Bohy *et al.* (2015) and Tapia *et al.* (2019) in particular for the smaller  $\phi$ -range.

The log–log plots shown in the insets of figure 10 are made to analyse the asymptotic behaviours close to the jamming transition. The data for  $\eta_n$  coming from run Re8 in the inset of figure 10(b) present a divergence in  $(1 - \phi / \phi_c)^{-2}$ , in agreement with previous work (see e.g. Boyer *et al.* 2011; Tapia *et al.* 2019); the other runs are too far from the jamming point to allow for any conclusions. The log–log plot shown in the inset of figure 10(a) reveals that the same divergence dominates close to jamming for  $\eta_s$ . This last point is also demonstrated by the finite value of  $\mu = \eta_s / \eta_n$  at vanishing  $J$  for the data coming from run Re8 and from the erosion experiments in figure 8(a).

Apart from the difficult task to accurately measure within the sediment transport layer of only a couple particle diameters thickness, the issues described above to recover the rheological quantities at large  $J$  and small  $\phi$  can be attributed to the fact that sediment transport can be sub-divided into two different regimens (Revil-Baudard *et al.* 2015). On the one hand, the dynamics of dense suspensions with large  $\phi$  is dominated by frictional contact. In fact, this is the regime that has been investigated in the experiments of Boyer *et al.* (2011), Dagois-Bohy *et al.* (2015) and Tapia *et al.* (2019) and for which the empirical

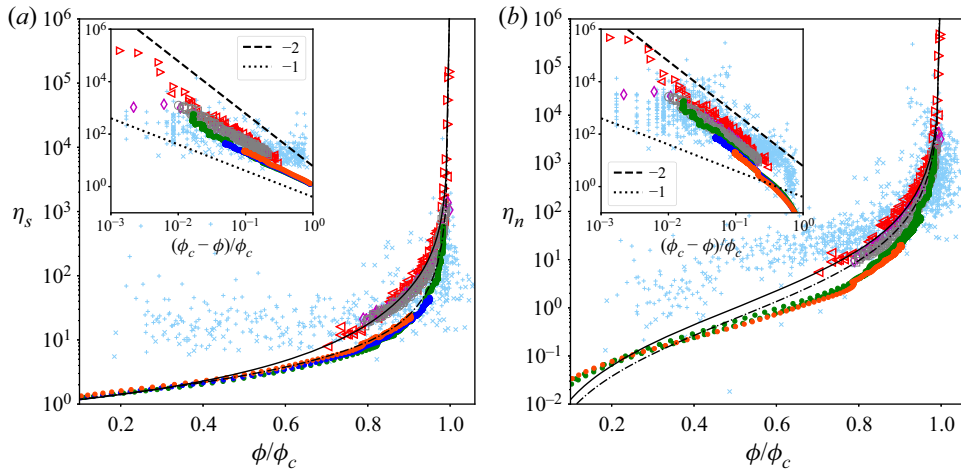


Figure 10. (a) Shear,  $\eta_s = \tau/\eta_f\dot{\gamma}$ , and (b) normal,  $\eta_n = p_p/\eta_f\dot{\gamma}$ , viscosities vs the scaled volume fraction  $\phi/\phi_c$ . Same comparisons as in figure 9.

correlations shown in figures 9 and 10 have been derived. On the other hand, low volume fractions represent the dilute regime of mostly binary collisions between particles. It was therefore concluded by Maurin, Chauchat & Frey (2016) that those empirical correlations may need adjustments for these flow conditions.

Hence, our observations are in line with the study of Houssais *et al.* (2016), who conducted experiments of sediment transported in an annular flume and measured depth-resolved profiles very similar to the data presented here. In this study, the authors had to introduce a confinement pressure to correct  $\mu$  for large values of  $J$ . This pressure was added to the granular pressure and can be interpreted as the artificial weight of the top plate in a pressure-imposed rheometer. Houssais *et al.* (2016) found good agreement with the correlations of Boyer *et al.* (2011) for  $\mu(J)$  using this measure, but unfortunately, the agreement for the correlation  $\phi(J)$  was not as good in that study. As already mentioned in §4.2, we omit using this strategy of an additional confinement pressure in the present analysis. The high resolution of the numerical data did not require such a treatment, because all relevant quantities could be recovered by our statistical analysis in a straightforward manner. This way, we ensure to stay consistent with the two-phase flow model (2.1) and (2.2) from Aussillous *et al.* (2013). The same applies for the revisited data of Aussillous *et al.* (2013), but for these data we use the additional assumption of  $u_f = u_{p,in}$  to reconstruct the fluid velocity profile from a mixed Couette–Poiseuille flow, which yields a slight underestimation of the fluid velocity in the range of large  $J$  and low  $\phi$ .

To further investigate the governing effects in both the dilute and the dense regime as a function of the particle volume fraction, we make use of the highly resolved data and the stress balance (4.4) derived in §4 and separate the stresses due contact and hydrodynamic interaction. These are plotted in figure 11 (without the normalisation by  $\phi_c$ ) together with a comparison of the data of Gallier *et al.* (2014), who carried out three-dimensional simulations of neutrally buoyant, non-Brownian, frictional spheres in a Couette cell of constant size, i.e. volume-imposed rheometry. For our simulation results, the data of the three simulation runs collapse onto a single master curve for both the contact and the hydrodynamic stress components. For  $\phi > 0.3$ , there are no significant long-range hydrodynamic effects possible and the particle contact is the main contribution

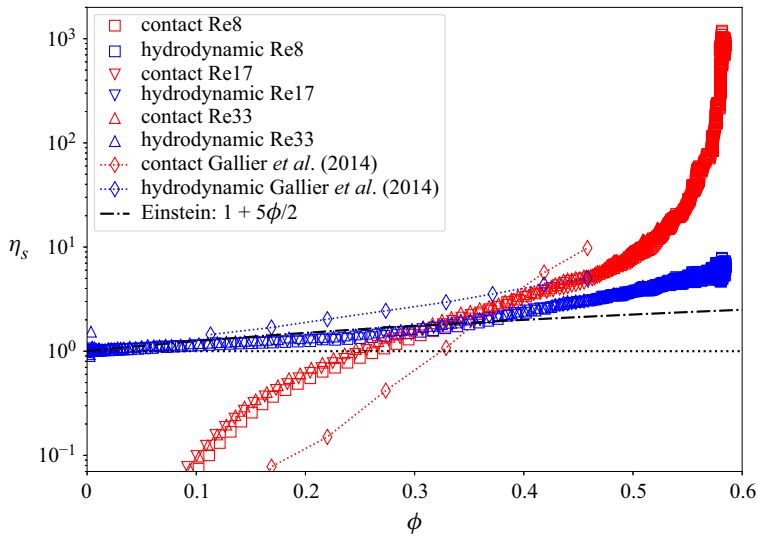


Figure 11. Relative contributions of the frictional contact (red) and the hydrodynamic (blue) stress to  $\eta_s$ .

to the total stress, whereas hydrodynamic effects prevail below this threshold value of  $\phi$ . The analysis therefore reveals the reason why the considerations for pressure-imposed rheometry also hold for sediment transport in the dense regime, i.e.  $\phi > 0.3$ , where the rheology is dominated by particle contact.

In the dilute regime, i.e.  $\phi < 0.3$ , the hydrodynamic component scales very well with the Einstein relation  $\eta_s = 1 + \frac{5}{2}\phi$  (Einstein 1956) and the contribution from particle contact becomes negligible. Our analysis furthermore shows that the deviation of the hydrodynamic component from its clear fluid value ( $\eta_s = 1$ ) is induced by the lubrication forces (not shown here). This observation differs from the simulation results of Gallier *et al.* (2014) obtained using volume-imposed rheometry for  $0.1 \leq \phi \leq 0.45$ , where particles are distributed homogeneously in the simulation domain. In the present simulations, the dilute regime represents the thin layer of active sediment transport, where particles are still touching and aligned in the shearing direction so that the particle volume fraction decreases rapidly from densely packed to zero within a thin layer that is only a couple of diameters thick. Hence, long-range hydrodynamic effects are screened by the highly anisotropic distribution and the steep gradient of  $\phi$  in this layer. As a result, the hydrodynamic component resembles a porous medium flow behaviour, as anticipated in the two-phase modelling of Ouriemi *et al.* (2009) and Aussillous *et al.* (2013).

To the knowledge of the authors, the only numerical study of particle-resolved DNS that was able to perform the analysis of the rheological behaviour of a sheared sediment bed has been presented by Kidanemariam (2016), who has carried out a total of 24 simulation runs with varying Reynolds and Galileo numbers in the laminar flow regime. Interestingly, this study also deviates from the empirical correlations of Boyer *et al.* (2011) by overestimating  $\mu(J)$  and underestimating  $\phi(J)/\phi_c$  for large  $J$ , whereas our simulation data overestimate the volume fraction in this regime (cf. figure 9b). The low values of  $\phi$  for large  $J$  in the data of Kidanemariam (2016) can in parts be attributed to the difference in handling particle collisions and contact. Kidanemariam (2016) did not resolve lubrication forces, which imposes the constraint that one has to keep a minimum distance between the particles. Consequently, the granular packing has to be less dense so that unusually low values of  $0.43 \leq \phi_c \leq 0.53$  were reported for the maximum packing fraction. Hence, the data and

the analysis presented here demonstrate a substantial improvement over previous efforts to capture the rheology of sediment beds over a wide range of  $J$ .

## 6. Concluding remarks

Serving the need to use constitutive laws for macroscopic sediment transport models, the present paper introduced a new means to generate highly resolved data for the rheological behaviour of granular sediment beds sheared by a viscous, pressure-driven flow. The rheology is assessed by a statistical analysis to extract the physical quantities needed to compute the rheological parameters. The highly resolved simulations provide the data needed to assess the stress exchange of the fluid–particle mixture by deriving the stress balance from first principles. To better understand naturally occurring sediment-laden flows in pipes and rivers, we focus on pressure-driven flows, where the total stress increases with flow depth. The analysis verified the conceptual two-phase model of Ouriemi *et al.* (2009) and Aussillous *et al.* (2013) that has been derived from the Brinkman equations, and deduces the total fluid shear and the granular pressure as the relevant rheological quantities. We compare our numerical results to the rheology of corresponding experiments by revisiting the data set of pressure-driven flows investigated by Aussillous *et al.* (2013) and found reasonably good agreement between the numerical and experimental data. The results presented here clearly show that sediment transport by pressure-driven flows yields results that are similar to those of previous studies of annular Couette-type flows, even though these studies were conducted with dense suspensions of neutrally buoyant particles in pressure-imposed rheometers. The analysed data agree well with the empirical correlations of Boyer *et al.* (2011) and Morris & Boulay (1999) derived therefrom. In the more dilute regime, the simulation data fall in between the bounds set by those two extrapolated correlations. The good agreement of the data obtained from pressure driven flows with those from Couette flows potentially justifies the use of these empirical correlations as constitutive equations for two-phase flow solvers for sediment transport applications in the dense regime. Separating the total shear stress of our simulation results into the parts from hydrodynamic interaction and particle contact revealed a critical particle volume fraction of  $\phi \approx 0.3$ , for which particle contact becomes the dominant component, so that classical empirical relations from rheometry become applicable. In the dilute regime, we obtain a scaling in agreement with the Einstein relation, which illustrates a flow behaviour that differs from classical rheometry studies, because the long-range interactions are screened by the porous medium. This effect corresponds to the thin layer of sediment transport over which hydrodynamic and contact stresses but also  $\phi$  vary rapidly, which is very difficult to grasp, but it constitutes the main difference between classical rheometry of neutrally buoyant suspensions and the rheology of sediment transport. More work of this kind will be needed in the future to address different particle properties in complementary experimental and numerical campaigns and flow situations that are more complex than the two fundamental flow types Couette and Poiseuille flow.

**Supplementary material.** Supplementary material is available at <https://doi.org/10.1017/jfm.2021.457>. The rheological data of figures 8, 9, 10 and 11 are given as supplementary materials available at <https://doi.org/10.1017/jfm.2021.457>.

**Funding.** B.V. gratefully acknowledges the Feodor-Lynen scholarship provided by the Alexander von Humboldt foundation (Germany) and the German Research Foundation (DFG) grant VO2413/2-1. Furthermore, this research was supported in part by the Department of Energy Office of Science Graduate Fellowship Program (DOE SCGF), made possible in part by the American Recovery and Reinvestment Act of 2009, administered by ORISE-ORAU under contract no. DE-AC05-06OR23100. It is also supported by the Petroleum



Research Fund, administered by the American Chemical Society, grant number 54948-ND9. E.M. gratefully acknowledges support through NSF grants CBET-1803380 and OCE-1924655, as well as by the Army Research Office through grant W911NF-18-1-0379 and from Petrobras. Computational resources for this work used the Extreme Science and Engineering Discovery Environment (XSEDE), which is supported by the National Science Foundation, USA, grant no. ACI-1548562. This work was supported by the Labex MEC (ANR-10-LABX-0092) under the A\*MIDEX project (ANR-11-IDEX-0001-02) funded by the French government programme Investissements d'Avenir.

**Declaration of interests.** The authors report no conflict of interest.

**Author ORCIDs.**

✉ B. Vowinckel <https://orcid.org/0000-0001-6853-7750>;

✉ E. Biegert <https://orcid.org/0000-0002-7606-1921>;

✉ E. Meiburg <https://orcid.org/0000-0003-3670-8193>;

✉ P. Aussillous <https://orcid.org/0000-0002-3806-1293>;

✉ É. Guazzelli <https://orcid.org/0000-0003-3019-462X>.

REFERENCES

- ALLEN, B. & KUDROLLI, A. 2017 Depth resolved granular transport driven by shearing fluid flow. *Phys. Rev. Fluids* **2** (2), 024304.
- AUSSILLOUS, P., CHAUCHAT, J., PAILHA, M., MÉDALE, M. & GUAZZELLI, É. 2013 Investigation of the mobile granular layer in bedload transport by laminar shearing flows. *J. Fluid Mech.* **736**, 594–615.
- BAGNOLD, R.A. 1954 Experiments on a gravity-free dispersion of large solid spheres in a Newtonian fluid under shear. *Proc. R. Soc. Lond. A* **225** (1160), 49–63.
- BAGNOLD, R.A. 1956 The flow of cohesionless grains in fluids. *Phil. Trans. R. Soc. Lond. A* **249** (964), 235–297.
- BIEGERT, E., VOWINCKEL, B., HUA, L. & MEIBURG, E. 2018 Stress balance for a viscous flow with a single rolling particle. In *E3S Web of Conferences, River Flow 2018*, vol. 40, 04003. E3S Web of Conferences.
- BIEGERT, E., VOWINCKEL, B. & MEIBURG, E. 2017a A collision model for grain-resolving simulations of flows over dense, mobile, polydisperse granular sediment beds. *J. Comput. Phys.* **340**, 105–127.
- BIEGERT, E., VOWINCKEL, B., OUILLOU, R. & MEIBURG, E. 2017b High-resolution simulations of turbidity currents. *Prog. Earth Planet. Sci.* **4** (1), 33.
- BIEGERT, E.K. 2018 Eroding uncertainty: towards understanding flows interacting with mobile sediment beds using grain-resolving simulations. PhD thesis, University of California, Santa Barbara.
- BOYER, F., GUAZZELLI, É. & POULIQUEN, O. 2011 Unifying suspension and granular rheology. *Phys. Rev. Lett.* **107** (18), 1–5.
- COX, R. & BRENNER, H. 1967 The slow motion of a sphere through a viscous fluid towards a plane surface. Small gap widths, including inertial effects. *Chem. Engng Sci.* **22**, 1753–1777.
- DAGOIS-BOHY, S., HORMOZI, S., GUAZZELLI, É. & POULIQUEN, O. 2015 Rheology of dense suspensions of non-colloidal spheres in yield-stress fluids. *J. Fluid Mech.* **776**, R2.
- DIJKSMAN, J.A., RIETZ, F., LŐRINCZ, K.A., VAN HECKE, M. & LOSERT, W. 2012 Invited article: refractive index matched scanning of dense granular materials. *Rev. Sci. Instrum.* **83** (1), 011301.
- EINSTEIN, A. 1956 *Investigations on the Theory of the Brownian Movement*. Courier Corporation.
- FOERSTER, S.F., LOUGE, M.Y., CHANG, H. & ALLIA, K. 1994 Measurements of the collision properties of small spheres. *Phys. Fluids* **6** (3), 1108.
- FORTERRE, Y. & POULIQUEN, O. 2008 Flows of dense granular media. *Annu. Rev. Fluid Mech.* **40**, 1–24.
- GALLIER, S., LEMAIRE, E., LOBRY, L. & PETERS, F. 2014 A fictitious domain approach for the simulation of dense suspensions. *J. Comput. Phys.* **256**, 367–387.
- GALLIER, S., PETERS, F. & LOBRY, L. 2018 Simulations of sheared dense noncolloidal suspensions: evaluation of the role of long-range hydrodynamics. *Phys. Rev. Fluids* **3** (4), 042301.
- GDR MIDI 2004 On dense granular flows. *Eur. Phys. J. E* **14** (4), 314–365.
- GOLDHIRSCH, I. 2010 Stress, stress asymmetry and couple stress: from discrete particles to continuous fields. *Granul. Matt.* **12** (3), 239–252.
- GONDRET, P., LANCE, M. & PETIT, L. 2002 Bouncing motion of spherical particles in fluids. *Phys. Fluids* **14** (2), 643–652.
- GUAZZELLI, É. & POULIQUEN, O. 2018 Rheology of dense granular suspensions. *J. Fluid Mech.* **852**, P1.

## *Rheology of sediment beds sheared by pressure-driven flows*

- HOUSSAIS, M., ORTIZ, C.P., DURIAN, D.J. & JEROLMACK, D.J. 2016 Rheology of sediment transported by a laminar flow. *Phys. Rev. E* **94** (6), 062609.
- JAIN, R., VOWINCKEL, B. & FRÖHLICH, J. 2017 Spanwise particle clusters in DNS of sediment transport over a regular and an irregular bed. *Flow Turbul. Combust.* **99** (3–4), 973–990.
- JENKINS, J.T. & LARCHER, M. 2017 Dense, layered, inclined flows of spheres. *Phys. Rev. Fluids* **2** (12), 1–14.
- JEROLMACK, D.J. & DANIELS, K.E. 2019 Viewing earth's surface as a soft-matter landscape. *Nat. Rev. Phys.*, 1–15.
- JOSEPH, G.G. & HUNT, M.L. 2004 Oblique particle-wall collisions in a liquid. *J. Fluid Mech.* **510**, 71–93.
- KEMPE, T. & FRÖHLICH, J. 2012a An improved immersed boundary method with direct forcing for the simulation of particle laden flows. *J. Comput. Phys.* **231** (9), 3663–3684.
- KEMPE, T. & FRÖHLICH, J. 2012b Collision modelling for the interface-resolved simulation of spherical particles in viscous fluids. *J. Fluid Mech.* **709**, 445–489.
- KIDANEMARIAM, A. 2016 *The Formation of Patterns in Subaqueous Sediment*. Karlsruhe Institute of Technology.
- KIDANEMARIAM, A.G. & UHLMANN, M. 2014 Interface-resolved direct numerical simulation of the erosion of a sediment bed sheared by laminar channel flow. *Intl J. Multiphase Flow* **67**, 174–188.
- LAJEUNESSE, E., MALVERTI, L., LANCIEN, P., ARMSTRONG, L., MÉTIVIER, F., COLEMAN, S., SMITH, C.E., DAVIES, T., CANTELLI, A. & PARKER, G. 2010 Fluvial and submarine morphodynamics of laminar and near-laminar flows: a synthesis. *Sedimentology* **57** (1), 1–26.
- LOBKOVSKY, A.E., ORPE, A.V., MOLLOY, R., KUDROLLI, A. & ROTHMAN, D.H. 2008 Erosion of a granular bed driven by laminar fluid flow. *J. Fluid Mech.* **605**, 47–58.
- MAURIN, R., CHAUCHAT, J. & FREY, P. 2016 Dense granular flow rheology in turbulent bedload transport. *J. Fluid Mech.* **804**, 490–512.
- MORRIS, J.F. & BOULAY, F. 1999 Curvilinear flows of noncolloidal suspensions: the role of normal stresses. *J. Rheol.* **43** (5), 1213–1237.
- MOULLERON, H., CHARRU, F. & EIFF, O. 2009 Inside the moving layer of a sheared granular bed. *J. Fluid Mech.* **628**, 229.
- NESS, C. & SUN, J. 2015 Shear thickening regimes of dense non-Brownian suspensions. *Soft Matt.* **12**, 914–924.
- NIKORA, V., BALLIO, F., COLEMAN, S. & POKRAJAC, D. 2013 Spatially averaged flows over mobile rough beds: definitions, averaging theorems, and conservation equations. *ASCE J. Hydraul. Engng* **139** (8), 803–811.
- OURIEMI, M., AUSSILLOUS, P. & GUAZZELLI, É. 2009 Sediment dynamics. Part 1. Bed-load transport by laminar shearing flows. *J. Fluid Mech.* **636** (1940), 295–319.
- REUIL-BAUDARD, T., CHAUCHAT, J., HURTHUR, D. & BARRAUD, P.-A. 2015 Investigation of sheet-flow processes based on novel acoustic high-resolution velocity and concentration measurements. *J. Fluid Mech.* **767**, 1–30.
- ROMA, A., PESKIN, C. & BERGER, M. 1999 An adaptive version of the immersed boundary method. *J. Comput. Phys.* **153** (2), 509–534.
- STICKEL, J.J. & POWELL, R.L. 2005 Fluid mechanics and rheology of dense suspensions. *Annu. Rev. Fluid Mech.* **37** (1), 129–149.
- TAPIA, F., POULIQUEN, O. & GUAZZELLI, É. 2019 Influence of surface roughness on the rheology of immersed and dry frictional spheres. *Phys. Rev. Fluids* **4** (10), 104302.
- TEN CATE, A., DERKSEN, J.J., PORTELA, L.M. & VAN DEN AKKER, H.E.A. 2004 Fully resolved simulations of colliding monodisperse spheres in forced isotropic turbulence. *J. Fluid Mech.* **519**, 233–271.
- THORNTON, C., CUMMINS, S.J. & CLEARY, P.W. 2011 An investigation of the comparative behaviour of alternative contact force models during elastic collisions. *Powder Technol.* **210** (3), 189–197.
- THORNTON, C., CUMMINS, S.J. & CLEARY, P.W. 2013 An investigation of the comparative behaviour of alternative contact force models during inelastic collisions. *Powder Technol.* **233**, 30–46.
- UHLMANN, M. 2005 An immersed boundary method with direct forcing for the simulation of particulate flows. *J. Comput. Phys.* **209** (2), 448–476.
- VOWINCKEL, B. 2021 Incorporating grain-scale processes in macroscopic sediment transport models. *Acta Mechanica* **232**, 2023–2050.
- VOWINCKEL, B., BIEGERT, E., LUZZATTO-FEGIZ, P. & MEIBURG, E. 2019 Consolidation of freshly deposited cohesive and noncohesive sediment: particle-resolved simulations. *Phys. Rev. Fluids* **4** (7), 074305.
- VOWINCKEL, B., KEMPE, T. & FRÖHLICH, J. 2014 Fluid–particle interaction in turbulent open channel flow with fully-resolved mobile beds. *Adv. Water Resour.* **72**, 32–44.

*B. Vowinckel and others*

- VOWINCKEL, B., NIKORA, V., KEMPE, T. & FRÖHLICH, J. 2017*a* Momentum balance in flows over mobile granular beds: application of double-averaging methodology to DNS data. *J. Hydraul. Res.* **55** (2), 190–207.
- VOWINCKEL, B., NIKORA, V., KEMPE, T. & FRÖHLICH, J. 2017*b* Spatially-averaged momentum fluxes and stresses in flows over mobile granular beds: a DNS-based study. *J. Hydraul. Res.* **55** (2), 208–223.
- WEINHART, T., THORNTON, A.R., LUDING, S. & BOKHOVE, O. 2012 From discrete particles to continuum fields near a boundary. *Granul. Matt.* **14** (2), 289–294.